PCCP

PAPER

View Article Online
View Journal | View Issue

Cite this: *Phys. Chem. Chem. Phys.*, 2022, **24**, 22115

Construction and performance of OLED devices prepared from liquid-crystalline TADF materials†

Alfiya F. Suleymanova,[a] Marsel Z. Shafikov,[b] Xinrui Chen,[c] Yafei Wang,*[c] Rafal Czerwieniec*[b] and Duncan W. Bruce*[a]

Received 13th June 2022,
Accepted 28th August 2022

DOI: 10.1039/d2cp02684h

rsc.li/pccp

The device performance is reported for three compounds which show both thermally activated delayed fluorescence and liquid crystallinity, and use the donor 3,6-bis(3,4-didodecyloxyphenyl)carbazole. Two of the compounds, whose photophysics were reported previously, are based on a terephthalonitrile acceptor. A third and new compound is based on an isophthalonitrile acceptor and shows a more temperature-accessible mesophase and enhanced solution emission quantum yield. Two of the compounds show device external quantum efficiencies of between 2–3% and exhibit very small efficiency roll off. The responses are evaluated in terms of the specific nature of the materials.

Introduction

Luminescent liquid-crystalline (LC) materials are of great interest due to their unique combination of properties, as they self-organise into anisotropic structures and are able to produce circularly and linearly polarised light that is attractive for use in optical devices.[1–7] Also, liquid crystals forming columnar phases have been recognised as an attractive class of photoconductors due to their anisotropic charge-transporting ability.[8–11]

Recently, there has been increasing interest in thermally activated delayed fluorescent (TADF) materials showing up to 100% of internal quantum efficiency without the need for a heavy transition metal such as iridium.[12–14] This is due to the design of molecules with a minimised energy gap between the lowest excited singlet (S_1) and triplet (T_1) states, thereby promoting efficient reverse intersystem crossing (rISC) from the non-radiative triplet state to the radiative singlet state.[15,16] Although TADF as a phenomenon has been known for many decades,[17–19] it became very popular in application when Adachi and co-workers first demonstrated use of TADF molecules in organic light-emitting diodes (OLEDs).[20–22] Today, these materials are used in many different areas such as time-resolved fluorescence imaging,[23–27] organic photocatalysis,[28–31] photodynamic therapy[32–35] and in improving the efficiency of OLED devices.[36,37]

Constructing molecules exhibiting both LC and TADF properties is an interesting approach for potential application in OLED devices and, for example, there is a very recent report of LC properties in some disc-like, multi-resonant TADF materials.[38] Some of us have previously reported LCs based on dihydroacridine donor and diphenylsulfone acceptor, which show external quantum efficiencies in devices of up to 15%,[39] whereas in another, earlier study, we reported multifunctional materials based on carbazole-substituted terephthalonitriles (Fig. 1, **1**, **2**).[40] In this latter work, modification of well-known donor–acceptor systems[14] led to the combination of TADF and LC properties in one material, but the contribution of TADF to the overall emission was only 5–10% and the emission quantum yields of the materials were low. Nonetheless, we were keen to investigate the behaviour of these materials in device constructs, which we now report along with studies on a new LC TADF emitter (**3**) based on isophthalonitrile and a carbazole and showing increased quantum yield and TADF contribution.

Results and discussion

Compound **3**, which is based on the well-known emitter 4CzIPN,[20] was prepared following a slightly modified literature method by coupling commercially available tetrafluoroisophthalonitrile with the sodium salt of 3,6-bis(3,4-didocylocyphenyl)carbazole (Scheme 1). The carbazole was synthesised by using a method described earlier.[40]

Liquid-crystalline properties

Polarised optical microscopy, differential scanning calorimetry (DSC) and small-angle X-ray scattering (SAXS) were used to determine the liquid-crystalline properties of **3**. Starting at

[a] *Department of Chemistry, University of York, Heslington, YORK YO10 5DD, UK. E-mail: duncan.bruce@york.ac.uk; Tel: (+44) 1904 324085*
[b] *Institut für Physikalische Chemie, Universität Regensburg, Universitätsstrasse 31, 93053 Regensburg, Germany. E-mail: rafal.czerwieniec@chemie.uni-regensburg.de; Tel: (+49) 941 943 4463*
[c] *School of Materials Science & Engineering, Changzhou University, Changzhou 213164, P. R. China. E-mail: qiji830404@hotmail.com*

† Electronic supplementary information (ESI) available. See DOI: https://doi.org/10.1039/d2cp02684h

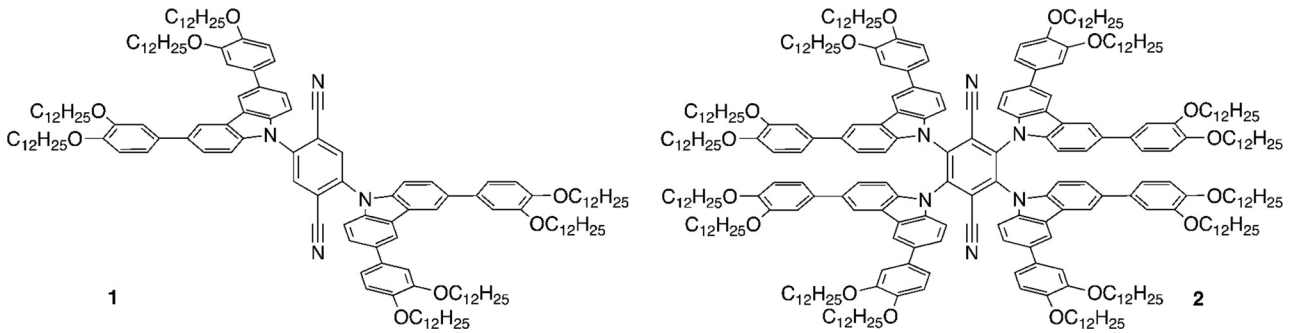

Fig. 1 Previously prepared liquid-crystalline TADF materials.

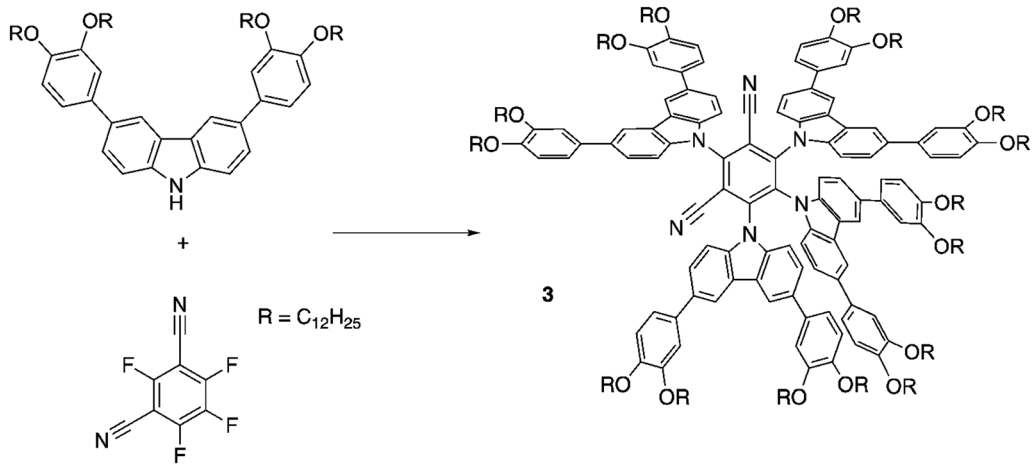

Scheme 1 Synthesis of 2,4,5,6-tetra(3,6-bis-(3,4-didodecyloxybenzene)carbazolyl)-1,3-dicyanobenzene (**3**). Reagents: NaH, 3,6-bis(3,4-didodecyloxybenzene)carbazole, THF, reflux, 2 h; 2,4,5,6-tetrafluoro-1,4-dicyanobenzene in THF, reflux, 10 minutes, 32%.

room temperature, optical microscopy showed the presence of soft solid whose viscosity gradually reduced until it cleared into the isotropic phase at 76 °C (DSC traces for three heat–cool scans are found as Fig. S3, ESI†). Then, on cooling, a liquid-crystalline texture, typical of a columnar hexagonal mesophase (Col_h), appeared immediately at 75.9 °C (Fig. 2a). SAXS (Fig. 2b) shows only a single reflection at 2θ = 2.66° corresponding to a spacing of 33.17 Å and, while this is

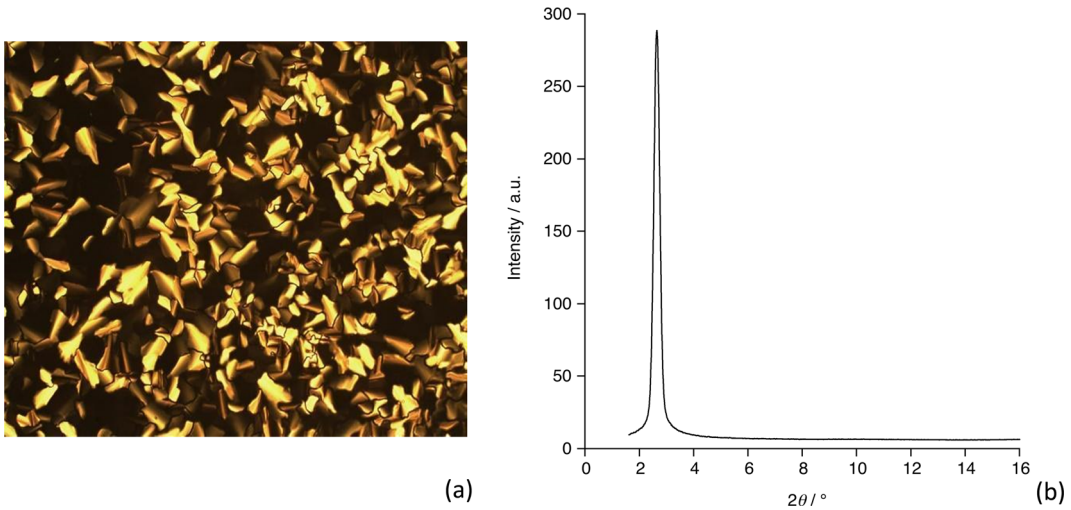

Fig. 2 (a) Polarising optical microscopy image of **3** at 76 °C on cooling (magnification 20×) and (b) small-angle diffraction pattern recorded at 63.7 °C.

insufficient to identify the mesophase, when coupled with the optical texture and the presence of some homeotropic areas then we are confident in the phase assignment. Based on that assumption, the hexagonal lattice parameter is 38.3 Å and this distance varies between 38.9 and 37.7 Å over the temperature range 45.5 to 69.8 °C (smaller spacing at the highest temperature). Upon further cooling, the system does not crystallise, but rather appears to form a glass. DSC measurements confirm the clearing transition temperature obtained from optical observations and show evidence of a glass transition on cooling at *ca.* 35 °C, which reverses on heating. There is also a weak endothermic event on heating at 53.4 °C, which may correspond to the melting of a small portion of the material that crystallised (Fig. S3, ESI†). There being no apparent melting point observed it is assumed that the material obtained from solution is already in the columnar mesophase. Compared to compounds **1** and **2** which clear at 181 and 191 °C, respectively,[40] compound **3** clears at a very much lower temperature, which is attributed to its lower symmetry, in turn leading to much less efficient packing in the solid state.[41,42] The phase behaviour may, therefore, be summarised as shown below. The endothermic event is not ascribed as melting in the absence of confirmatory evidence.

$$g \bullet 35 \bullet Col_h \bullet 76 \bullet Iso$$

Photophysical properties

The optical properties of compound **3** are characteristic of purely organic TADF materials. The absorption spectrum measured for a dilute toluene solution features an intense band centred at about 300 nm and broader band at longer wavelength and about an order of magnitude less intense. The intense band is assigned to local $\pi \rightarrow \pi^*$ transition within the carbazole derivatives. The broad nature and low intensity of the lower energy absorption band is characteristic of transitions of charge-transfer character, and is therefore assigned as transitions from the carbazole derivatives to the isophthalonitrile acceptor unit. It is noted that this band covers at least two transitions centred at about 410 nm and 500 nm (Fig. 3) indicating that the molecule has several different charge-transfer excited states. The emission spectrum of compound **3** in toluene has a broad, featureless shape with the maximum at about 590 nm which overlaps partially with the charge-transfer band of the absorption spectrum (Fig. 3). Such characteristics are all consistent with the emitting state(s) of the molecule also being charge transfer in character as expected for a donor–acceptor TADF material.

Time-correlated single photon counting (TCSPC) measurements in degassed toluene solution at room temperature reveal that the emission decay kinetics consist of a fast process with a decay time of 7.5 ns and a slower process with a decay time of 920 ns (Fig. 4). When re-measured following air-equilibration, the fast process does not show a notable change in kinetics whereas the decay time of the slower process shortens to 360 ns. Sensitivity of the decay rate to oxygen indicates the

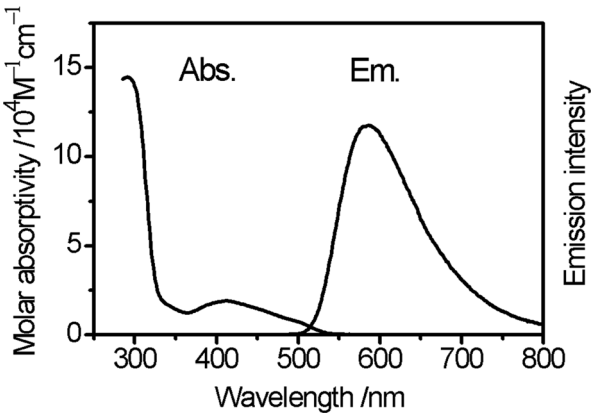

Fig. 3 UV-vis absorption and emission spectra of **3** in toluene measured at ambient temperature.

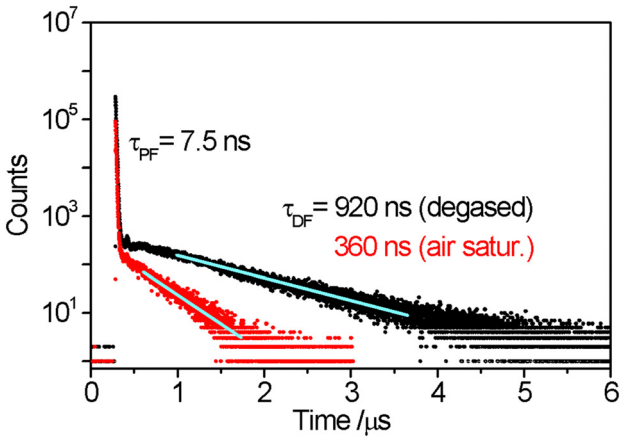

Fig. 4 Emission decay transients of (**3**) measured at ambient temperature in degassed and air-saturated toluene solution. Fitting exponential decay functions to the experimental decay data reveals decay times of prompt fluorescence (about 90% of integrated intensity) τ_{PF} = 7.5 ns and delayed emission τ_{PF} = 920 ns for degassed sample and τ_{DF}^{air} = 360 ns, respectively.

involvement of the triplet state, which can decay *via* Dexter-type energy transfer to molecular oxygen. On this basis, the shorter-lived component of emission is assigned to the prompt fluorescence ($S_1 \rightarrow S_0$) and the long-lived part to delayed fluorescent emission (also $S_1 \rightarrow S_0$) following $S_1 \rightarrow T_1$ intersystem crossing and the thermally activated reverse intersystem crossing (rISC) $T_1 \rightarrow S_1$, *i.e. via* thermalisation of the S_1 and T_1 states. It is noted that the contribution of $T_1 \rightarrow S_0$ phosphorescence to the longer component is improbable as in purely organic materials it is typically observed only at low temperatures and characterised with decay times in the range of milliseconds and above. The overall emission quantum yield of compound **3** in degassed toluene at room temperature is 11% which is a notable increase when compared to the previously reported terephthalonitrile-based analogues **1** and **2** (Table 1). The integrated contribution of the TADF to the total emission intensity is about 10% which is also an increase compared to

Table 1 Photoluminescence data for **1–3**[a]

	λ_{em}/nm	φ_{PL}[b]	τ_{PF}/ns	τ_{DF}/s	k_{PF}[c]/s^{-1}	$k_{nr(S1)}$[d]	k_{ISC}[e]
1	560	5 (5)	6.9	3.5	0.6×10^7	1.5×10^8	$\geq 3.6 \times 10^5$
2	620	1.5	1.2	≤ 1	1.3×10^7	8.2×10^8	
3	585	11 (10)	7.5	0.92	1.3×10^7	$\leq 1.2 \times 10^8$	$\geq 1.5 \times 10^6$

[a] Data for **1** and **2** from ref. 39. [b] Values in parentheses represent percentile share of delayed emission intensity in the total quantum yield. [c] Calculated as $k_{PF} = \varphi_{PF}(S_1)/\tau_{PF}$. [d] Calculated as $k_{nr}(S_1) = (1 - (\varphi_{PF} + \varphi_{DF})/\tau_{PF}$, *e.g.*, assuming that all non-radiative relaxation to the ground state occurs *via* the $S_1 \rightarrow S_0$ pathway, thus representing the upper limit. [e] Calculated as $k_{ISC} = \varphi_{DF}/\tau_{PF}$, *e.g.*, assuming that all non-radiative relaxation to the ground state occurs *via* the $S_1 \rightarrow S_0$ pathway, thus representing the lower limit.

compounds **1** and **2**, revealing the relative superiority of the molecular design of **3** as a TADF material.

Quantum chemical calculations

The electronic structure of **3** was computed at the M06[43]/def2-SVP[44] theory level utilising Gaussian 09 code.[45] Grimme's empirical dispersion correction (GD3)[46] was invoked to account for π–π interactions between carbazole units, and a polarisable continuum model C-PCM[47] with the parameters of toluene was included in the calculations to mimic the conditions of photophysical measurements. The molecular geometry of **3** was optimised in the singlet ground state (S_0) and at the lowest excited triplet state (T_1). The computations reveal that the π-conjugated systems of the three of the carbazole derivatives (Cz1, Cz2 and Cz3 in Fig. 5) in the molecule are stacked with interplanar distances of approximately 3.4–3.6 Å due to stabilising π–π interactions whereas, the carbazole derivative Cz4 is, of course, isolated (Fig. 5).

In the ground state (S_0), the planes of the carbazole groups stand oriented with respect to the plane of the isophthalonitrile acceptor at dihedral angles of 78.3° (Cz1), 78.3° (Cz2), 79.0° (Cz3) and 63.2° (Cz4). This separates the π systems of the carbazole derivatives (donors) and isophthalonitrile moiety (acceptor), which is a prerequisite for a small value for $\Delta E(S_1–T_1)$ and hence TADF behaviour. In the T_1 state, upon relaxation of the molecular geometry, the dihedral angle between the planes of the carbazole derivatives and of the isophthalonitrile moiety change slightly to 77.9° (Cz1), 76.5° (Cz2), 78.0° (Cz3), and increase by a few degrees to 68.9° (Cz4).

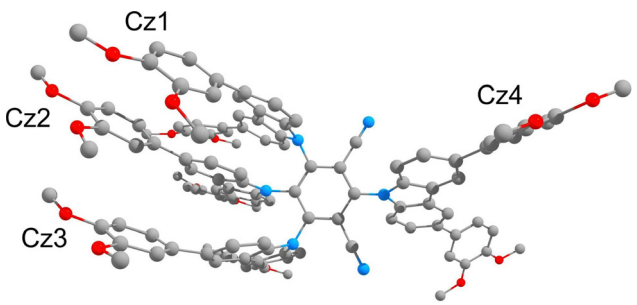

Fig. 5 Computed molecular structure of compound **3** in the ground state (S_0) geometry.

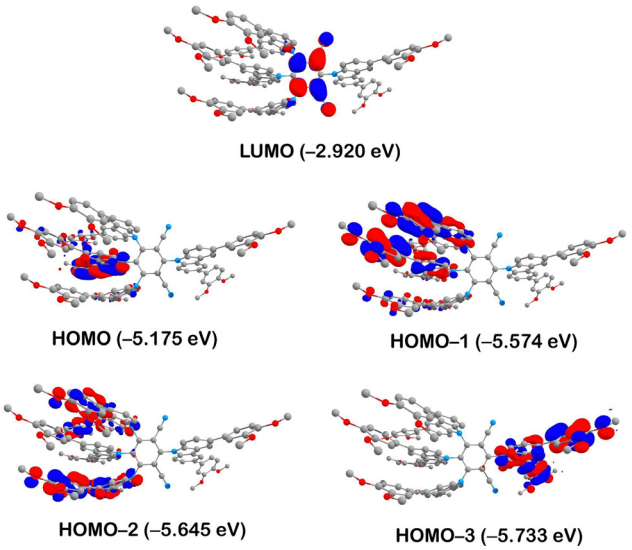

Fig. 6 Iso-surface contour plots (iso-value = 0.03) of selected molecular orbitals of compound **3** calculated at T_1 state geometry. Hydrogens are omitted for clarity.

According to TD-DFT calculations, conducted with a geometry optimised in the T_1 state, the S_1 and T_1 states originate from HOMO → LUMO transitions. The HOMO (−5.175 eV) is localised on the π–π-stacked carbazole units with the major contribution of Cz2 (84%) and minor contribution of Cz1 (7%) and Cz3 (8%). In contrast, the LUMO (−2.920 eV) is localised primarily on the iso-phthalonitrile moiety (93%) and has just 7% of the electron density on the two nitrogen-phenyl bonds of Cz1 and Cz3 (Fig. 6 and Table S1 in the ESI†). Thus, states S_1 and T_1 have predominantly charge-transfer character allowing for a weak exchange interaction and consequently a small value of the energy gap between them (S_1 = 1.632 eV and T_1 = 1.618 eV). Indeed, the calculated value of the gap is just $\Delta E(S_1–T_1)$ = 110 cm^{-1} (13.7 meV), indicating that the S_1 state can easily be populated at room temperature by thermal activation from T_1 through the rISC process. It is noted that although the computed excited state energies are underestimated in comparison to the experimental data, it probably has only a weak effect on the energy gap between them. The small computed $\Delta E(S_1–T_1)$ gap value agrees well with our assignment of the slow component of the TCSPC decay profile to TADF. It is also worth noting that, according to the TD-DFT calculations, the higher-lying excited states S_2/T_2 (HOMO−1 → LUMO) and S_3/T_3 (HOMO−2 → LUMO) are also charge transfer in character, originating from different carbazole groups in the molecule (Fig. 6). This is consistent with the absorption spectrum, which features >1 charge-transfer bands at longer wavelengths.

Comparing now compound **3** to the previously reported, isoelectronic compound **2** (Fig. 1), calculated at the same theory level, the latter has lower energies of both HOMO (−5.430 eV) and LUMO (−3.343 eV). The ΔE(HOMO–LUMO) energy gap, however, decreases from **3** (2.255 eV) to **2** (2.087 eV) as in **2** the relative stabilisation of the LUMO is greater than that of the HOMO. The larger ΔE(HOMO–LUMO) gap of **3** results in

relatively higher-lying S_1 and T_1 states as manifest by the blue shift of the emission from **2** (λ_{max} = 620 nm) to **3** (λ_{max} = 585 nm) accompanied by an increase in quantum yield according to the energy gap law.[48]

Notably, the π–π-stacking keeps the three carbazole units in **3** at much larger dihedral angles with respect to the isophthalonitrile, as compared to the analogous phthalonitrile based compound **1** (Fig. 1) where the dihedral angle is about 55° (computed at the same level of theory – see ESI† for computational data). Consequently, compound **1** has a much larger value of $\Delta E(S_1–T_1)$ = 1270 cm^{-1} (0.158 meV), resulting in less efficient thermal population of emissive S_1 states *via* rISC and more efficient, non-radiative $T_1 \rightarrow S_0$ relaxation. Thus, a higher emission quantum yield for **3** is observed, despite the lower energy of the emitting state (Table 1) compared to **1**.

The significantly higher ISC rate of **3**, compared to **1** (Table 1), also agrees with the importance of molecular vibrations within the π–π-stacked carbazole units. Such vibrations, displacing the atoms out of the conjugation plane of the carbazole groups, admix the σπ* and σπ* character to the primary ππ * character of S_1 and T_1 states. This enhances the spin–orbit coupling of the two states which will enhance the rates of $S_1 \leftrightarrow T_1$ ISC/rISC.[40,49]

The discussions presented above reveal the overall advantageous molecular design of **3** as a TADF material when compared to **1** and **2**.

Device performance

In order to evaluate the electroluminescent (EL) property of these liquid-crystalline TADF emitters, solution-processable OLEDs based on compounds **1**, **2** and **3** were fabricated with a configuration of ITO/PEDOT:PSS (40 nm)/host:*x* wt% (*x* = 1, 3 and 6) dopant (70 nm)/DPEPO (9 nm)/TmPyPB (45 nm)/LiF (0.5 nm)/Al (120 nm). In this device, a 7 : 3 blend of poly(9-vinylcarbazole) (PVK) and 1,3-bis[2-(4-*tert*-butylphenyl)-1,3,4-oxadiazo-5-yl]benzene (OXD-7) is used as the host. Poly(3,4-ethylenedioxythiophene):poly(styrenesulfonic acid) (PEDOT:PSS) is the hole-injection layer, while DPEPO and 1,3,5-tri(*m*-pyrid-3-yl-phenyl)benzene (TmPyPB) acted as the hole-blocking layer and electron-transport layer, respectively. LiF was the electron-injection material and Al served as the cathode. The device structure and molecular structures in the devices are shown in Fig. 7a and b, and the relevant EL data are summarised in Table 2.

As shown in the inset to Fig. 8a, all devices show broad EL spectra, similar to the PL profiles and, compared to compound **1**, compounds **2** and **3** exhibit red-shifted EL spectra owing to the greater number of donor moieties leading to a stabilisation of the HOMO. This is most pronounced in compound **2** where, in addition, the cyano acceptor groups are conjugated leading to emission at about 604 ± 6 nm. However, there is an additional emission band at about 420 nm for the device fabricated using compound **2**. This is assigned to the host matrix and implies incomplete energy transfer between host and emitter, suggesting inferior device performance.

As seen from Table 2, the EL spectra have a clear red shift with the increasing dopant concentration, moving between 10 and 12 nm from 1 to 6% doping. This is interpreted as reflecting the LC nature of the materials and the driving force to self-organise leading to relatively strong intermolecular interactions. In addition, the devices exhibit a relatively high turn-on voltage of around 8 V (@ 1 cd m^{-2}), which may be attributable to the rather high coverage of the periphery of the chromophore by flexible chains adversely affecting the carrier mobility (Fig. 8b). Thus, a passable device performance with an external quantum efficiency (EQE) of 2.97% is achieved for a device using compound **3** doped into the host at a concentration of 1 wt%, with a concomitant current efficiency of 7.69 cd A^{-1} and luminance of 1387 cd m^{-2}. Compound **1** has a not dissimilar efficiency of 2.29% at 1 wt% dopant, whereas compound **2** shows a much poorer EQE of 0.66%, also doped at 1 wt%. As expected, the device performance decreases with the increased dopant concentration due to the concentration quenching. Impressively however, the devices based on compounds **1** and **3** display a very small efficiency roll-off (Fig. 8a) with EQEs of 2.85 and 2.24% at 100 cd m^{-2} and 2.1 and 1.8% at 500 cd m^{-2}, respectively. These results demonstrate that both compounds **1** and **3** show very stable in the device.

Conclusion

By varying the isomerisation of a tetrakis(carbazoyl)benzenedinitrile from the terephthalonitrile (**1** and **2**) to an isophthalonitrile acceptor, a novel liquid-crystalline TADF emitter (**3**) was prepared. The

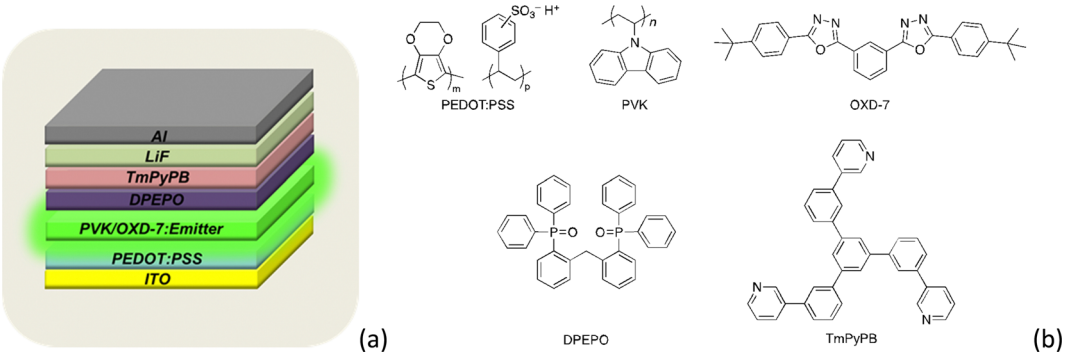

Fig. 7 (a) Scheme of device structure; (b) molecular structures in the device.

Table 2 Electroluminescent data for the devices

Compound	Dopant (wt%)	V_{on} (V)	L_{max} (cd m^{-2})	CE_{max} (cd A^{-1})	EQE_{max} (%)	CIE (x, y)	λ (nm)
1	1	8.0	994.5	6.82	2.29	(0.40, 0.54)	552
1	3	6.8	2065	6.58	2.19	(0.42, 0.53)	558
1	6	11.6	1148	2.00	0.76	(0.44, 0.52)	564
2	1	8.4	274.5	1.13	0.66	(0.53, 0.43)	598
2	3	6.8	407.2	1.20	0.59	(0.54, 0.41)	606
2	6	8.8	222.9	0.40	0.26	(0.56, 0.42)	610
3	1	8.0	1387	7.69	2.97	(0.48, 0.49)	578
3	3	8.4	1704	6.52	2.60	(0.49, 0.49)	578
3	6	10.4	837.1	3.27	1.50	(0.51, 0.48)	588

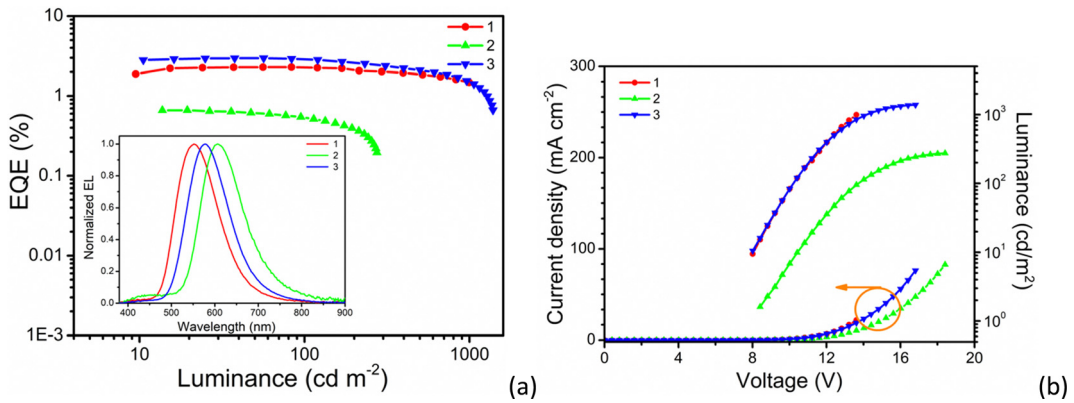

Fig. 8 Device performance at 1 wt% dopant concentration: (a) EQE-luminance curves (inset: the EL spectra); (b) J–V–L curves.

liquid crystal clearing point of the new material is very significantly reduced compared to its isomers (**1** and **2**) making its mesophase somewhat more accessible. This is directly attributable to the lower symmetry, which compromises the ability of the compounds to self-organise effectively so destabilising the liquid crystal phase.

Impressively, compound **3** showed enhanced emission quantum yield compared to compound **1** and **2**, leading to it showing the best device performance with an acceptable EQE_{max} value in a liquid crystalline-based TADF OLED and, in particular, the very small efficiency roll-off is a very pleasing observation. Nonetheless, in order to avoid concentration quenching, the loading of the emitter in the host is kept low (1–2%), which precludes the expression of the liquid crystal properties. However, in the only other study of LC-TADF materials in devices, 20 wt% loading of the luminophore were achieved,[39] which is a very encouraging observation and provides strong motivation to continue the development of LC-TADF emitters in order for the potentially advantageous properties, which include enhanced charge-transport, to be realised.

Conflicts of interest

There are no conflicts to declare.

Acknowledgements

The authors would like to thank the University of York (AFS), the Universität Regensburg (MZS) and the German Research Foundation (DFG) (Project No. 389797483) for financial support and the Royal Society (IEC\NSFC\181139) and the National Natural Science Foundation of China (51911530197, 51773021) for an International Exchange Award (DWB & YW). DWB would like to thank Dongyang Chen and Eli Zysman-Coleman (University of St Andrews University, UK) for enlightening discussions.

References

1 G. Qian, X. Yang, X. Wang, J. D. Herod, D. W. Bruce, S. Wang, W. Zhu, P. Duan and Y. Wang, *Adv. Opt. Mater.*, 2020, **8**, 2000775.
2 Y. Wang, J. Shi, J. Chen, W. Zhu and E. Baranoff, *J. Mater. Chem. C*, 2015, **3**, 7993–8005.
3 Y. Liu, L. H. You, F. X. Lin, K. Fu, W. Z. Yuan, E.-Q. Chen, Z.-Q. Yu and B. Z. Tang, *ACS Appl. Mater. Interfaces*, 2019, **11**, 3516–3523.
4 Q. Yang, J.-C. Zhu, Z.-X. Li, X.-S. Chen, Y.-X. Jiang, Z.-W. Luo, P. Wang and H.-L. Xie, *ACS Appl. Mater. Interfaces*, 2021, **13**, 26522–26532.
5 Y. Feng, H. Yu, D. Xie, Y. Zhu, X. Zhong, C. Pan and G. Shao, *Materials*, 2019, **12**, 1919.
6 J. De, W.-Y. Yang, I. Bala, S. P. Gupta, R. A. K. Yadav, D. K. Dubey, A. Chowdhury, J.-H. Jou and S. K. Pal, *ACS Appl. Mater. Interfaces*, 2019, **11**, 8291–8300.
7 V. S. Sharma, A. S. Sharma, N. K. Agarwal, P. A. Shah and P. S. Shrivastav, *Mol. Syst. Des. Eng.*, 2020, **5**, 1691–1705.

8 D. Adam, P. Schuhmacher, J. Simmerer, L. Häussling, K. Siemensmeyer, K. H. Etzbachi, H. Ringsdorf and D. Haarer, *Nature*, 1994, **371**, 141–143.
9 F. Closs, K. Siemensmeyer, T. Frey and D. Funhoff, *Liq. Cryst.*, 1993, **14**, 629–634.
10 A. Jankowiak, D. Pociecha, J. Szczytko, H. Monobe and P. Kaszyński, *J. Am. Chem. Soc.*, 2012, **134**, 2465–2468.
11 H. Iino, J.-I. Hanna and D. Haarer, *Phys. Rev. B: Condens. Matter Mater. Phys.*, 2005, **72**, 193203.
12 Z. Yang, Z. Mao, Z. Xie, Y. Zhang, S. Liu, J. Zhao, J. Xu, Z. Chi and M. P. Aldred, *Chem. Soc. Rev.*, 2017, **46**, 915–1016.
13 Y. Liu, C. Li, Z. Ren, S. Yan and M. R. Bryce, *Nat. Rev. Mater.*, 2018, **3**, 18020.
14 Y. Tao, K. Yuan, T. Chen, P. Xu, H. Li, R. Chen, C. Zheng, L. Zhang and W. Huang, *Adv. Mater.*, 2014, **26**, 7931–7958.
15 Y. Im, M. Kim, Y. J. Cho, J.-A. Seo, K. S. Yook and J. Y. Lee, *Chem. Mater.*, 2017, **29**, 1946–1963.
16 H. Yersin, R. Czerwieniec, M. Z. Shafikov and A. F. Suleymanova, *Chem. Phys. Chem.*, 2017, **18**, 3508–3535.
17 C. A. Parker and C. G. Hatchard, *Trans. Faraday Soc.*, 1961, **57**, 1894–1904.
18 C. A. Parker and C. G. Hatchard, *J. Phys. Chem.*, 1962, **66**, 2506–2511.
19 C. A. Parker and C. G. Hatchard, *Trans. Faraday Soc.*, 1963, **59**, 284–295.
20 H. Uoyama, K. Goushi, K. Shizu, H. Nomura and C. Adachi, *Nature*, 2012, **492**, 234–238.
21 A. Endo, M. Ogasawara, A. Takahashi, D. Yokoyama, Y. Kato and C. Adachi, *Adv. Mater.*, 2009, **21**, 4802–4806.
22 A. Endo, K. Sato, K. Yoshimura, T. Kai, A. Kawada, H. Miyazaki and C. Adachi, *Appl. Phys. Lett.*, 2011, **98**, 083302.
23 F. Ni, N. Li, L. Zhan and C. Yang, *Adv. Opt. Mater.*, 2020, **8**, 1902187.
24 F. Ni, Z. Zhu, X. Tong, M. Xie, Q. Zhao, C. Zhong, Y. Zou and C. Yang, *Chem. Sci.*, 2018, **9**, 6150–6155.
25 F. Ni, Z. Zhu, X. Tong, W. Zeng, K. An, D. Wei, S. Gong, Q. Zhao, X. Zhou and C. Yang, *Adv. Sci.*, 2019, **6**, 1801729.
26 S. Qi, S. Kim, V.-N. Nguyen, Y. Kim, G. Niu, G. Kim, S.-J. Kim, S. Park and J. Yoon, *ACS Appl. Mater. Interfaces*, 2020, **12**, 51293–51301.
27 X. Xiong, F. Song, J. Wang, Y. Zhang, Y. Xue, L. Sun, N. Jiang, P. Gao, L. Tian and X. Peng, *J. Am. Chem. Soc.*, 2014, **136**, 9590–9597.
28 M. A. Bryden and E. Zysman-Colman, *Chem. Soc. Rev.*, 2021, **50**, 7587–7680.
29 E. Speckmeier, T. G. Fischer and K. Zeitler, *J. Am. Chem. Soc.*, 2018, **140**, 15353–15365.
30 J. Luo and J. Zhang, *ACS Catal.*, 2016, **6**, 873–877.
31 Z.-J. Yu, W.-Y. Lou, H. Junge, A. Päpcke, H. Chen, L.-M. Xia, B. Xu, M.-M. Wang, X.-J. Wang, Q.-A. Wu, B.-Y. Lou, S. Lochbrunner, M. Beller and S.-P. Luo, *Catal. Commun.*, 2019, **119**, 11–15.
32 S. Hu, B. Huang, Y. Pu, C. Xia, Q. Zhang, S. Guo, Y. Wang and X. Huang, *J. Mater. Chem. B*, 2021, **9**, 5645–5655.
33 Z. Liu, W. Shi, G. Hong, W. Chen, B. Song, X. Peng, X. Xiong and F. Song, *J. Controlled Release*, 2019, **310**, 1–10.
34 J. Zhang, F. Fang, B. Liu, J. H. Tan, W. C. Chen, Z. Zhu, Y. Yuan, Y. Wan, X. Cui, S. Li, Q. X. Tong, J. Zhao, X. M. Meng and C. S. Lee, *ACS Appl. Mater. Interfaces*, 2019, **11**, 41051–41061.
35 Z. Liu, F. Song, W. Shi, G. Gurzadyan, H. Yin, B. Song, R. Liang and X. Peng, *ACS Appl. Mater. Interfaces*, 2019, **11**, 15426–15435.
36 Wisechip launches the world's first Hyperfluorescence™ OLED display – a 2.7 inch yellow PMOLED, **https://www.kyulux.com/wisechip-launches-the-worlds-first-hyperfluorescence-oled-display-a-2-7-inch-yellow-pmoled/**. Accessed 16-08-2022.
37 J. M. Ha, S. H. Hur, A. Pathak, J.-E. Jeong and H. Y. Woo, *NPG Asia Mater.*, 2021, **13**, 53.
38 D. Chen, F. T. Tenopala-Carmona, J. A. Knöller, A. Mischok, D. Hall, S. M. Suresh, T. Matulaitis, Y. Olivier, P. Nacke, F. Gießelmann, S. Laschat, M. C. Gather and E. Zysman-Colman, *ChemRxiv*, 2022, DOI: **10.26434/chemrxiv-2022-dc4zm**.
39 Y. Zhu, S. Zeng, B. Li, A. J. McEllin, J. Liao, Z. Fang, C. Xiao, D. W. Bruce, W. Zhu and Y. Wang, *ACS Appl. Mater. Interfaces*, 2022, **14**, 15437–15447.
40 A. F. Suleymanova, M. Z. Shafikov, A. C. Whitwood, R. Czerwieniec and D. W. Bruce, *J. Mater. Chem. C*, 2021, **9**, 6528–6535.
41 E. Voisin, E. Johan Foster, M. Rakotomalala and V. E. Williams, *Chem. Mater.*, 2009, **21**, 3251–3261.
42 E. J. Foster, J. Babuin, N. Nguyen and V. E. Williams, *Chem. Commun.*, 2004, 2052–2053, DOI: **10.1039/B400998C**.
43 Y. Zhao and D. G. Truhlar, *Theor. Chem. Acc.*, 2008, **120**, 215–241.
44 F. Weigend and R. Ahlrichs, *Phys. Chem. Chem. Phys.*, 2005, **7**, 3297–3305.
45 M. J. Frisch, G. W. Trucks, H. B. Schlegel, G. E. Scuseria, M. A. Robb, J. R. Cheeseman, G. Scalmani, V. Barone, B. Mennucci, G. A. Petersson, H. Nakatsuji, M. Caricato, X. Li, H. P. Hratchian, A. F. Izmaylov, J. Bloino, G. Zheng, J. L. Sonnenberg, M. Hada, M. Ehara, K. Toyota, R. Fukuda, J. Hasegawa, M. Ishida, T. Nakajima, Y. Honda, O. Kitao, H. Nakai, T. Vreven, J. A. Montgomery Jr., J. E. Peralta, F. Ogliaro, M. J. Bearpark, J. Heyd, E. N. Brothers, K. N. Kudin, V. N. Staroverov, R. Kobayashi, J. Normand, K. Raghavachari, A. P. Rendell, J. C. Burant, S. S. Iyengar, J. Tomasi, M. Cossi, N. Rega, N. J. Millam, M. Klene, J. E. Knox, J. B. Cross, V. Bakken, C. Adamo, J. Jaramillo, R. Gomperts, R. E. Stratmann, O. Yazyev, A. J. Austin, R. Cammi, C. Pomelli, J. W. Ochterski, R. L. Martin, K. Morokuma, V. G. Zakrzewski, G. A. Voth, P. Salvador, J. J. Dannenberg, S. Dapprich, A. D. Daniels, Ö. Farkas, J. B. Foresman, J. V. Ortiz, J. Cioslowski and D. J. Fox, *Gaussian 09*, Gaussian, Inc., Wallingford, CT, USA, 2009.
46 S. Grimme, J. Antony, S. Ehrlich and H. Krieg, *J. Chem. Phys.*, 2010, **132**, 154104.
47 M. Cossi, N. Rega, G. Scalmani and V. Barone, *J. Comput. Chem.*, 2003, **24**, 669–681.
48 R. Englman and J. Jortner, *Mol. Phys.*, 1970, **18**, 145–164.
49 M. A. El-Sayed, *J. Chem. Phys.*, 1963, **38**, 2834–2838.